Neuron, Vol. 35, 935–949, August 29, 2002, Copyright ©2002 by Cell Press

Conformational Switch between Slow and Fast Gating Modes: Allosteric Regulation of Voltage Sensor Mobility in the EAG K^+ Channel

Roland Schönherr,[1] Lidia M. Mannuzzu,[2] Ehud Y. Isacoff,[2,3] and Stefan H. Heinemann[1]

[1]Research Unit Molecular and Cellular Biophysics
Medical Faculty of the Friedrich Schiller University Jena
Drackendorfer Str. 1
D-07747 Jena
Germany

[2]Department of Molecular and Cell Biology
University of California at Berkeley
Berkeley, California 94720

Summary

Voltage-gated EAG K^+ channels switch between fast and slow gating modes in a Mg^{2+}-dependent manner by an unknown mechanism. We analyzed molecular motions in and around the voltage-sensing S4 in bEAG1. Using accessibility and perturbation analyses, we found that activation increases both the charge occupancy and volume of S4 side chains in the gating canal. Fluorescence measurements suggest that mode switching is due to a motion of the S2/S3 side of the gating canal. We propose that when S4 is in the resting state and its thin end is in the gating canal, a conformational rearrangement of S2/S3 narrows the canal around S4, forming the Mg^{2+} binding site. Binding of Mg^{2+} is proposed to stabilize this conformation and to slow opening of the gate by impeding S4's voltage-sensing outward motion.

Introduction

The function of most ion channels is controlled by physiological signals. These signals act on signal transduction devices that regulate molecular gates, which open and close the ion permeation pathway. In voltage-gated channels, the primary physiological signal is the membrane potential, which is monitored by voltage-sensing domains of the channel protein. Gating may be further regulated by secondary signals, which adjust channel activity to the physiological situation of the cell. For example, N-type and P/Q-type calcium channels switch from easily activated to "reluctant" modes of activation upon binding of $G\beta\gamma$ subunits (Ikeda, 1996; Herlitze et al., 1996; Herlitze et al., 2001). For many voltage-gated ion channels, gain setting is achieved by phosphorylation and dephosphorylation (reviewed by Jonas and Kaczmarek, 1996; Davis et al. 2001).

For ether à go-go potassium channels (EAG), two unique regulatory mechanisms are known to modulate gating properties: (1) Mg^{2+} ions in physiological concentrations switch channels from a fast to a slow mode of activation gating (Ludwig et al., 1994; Terlau et al., 1996; Tang et al., 2000), and (2) Ca^{2+}-calmodulin binding to a cytosolic C-terminal site reduces channel availability (Schönherr et al., 2000). In *Drosophila*, mutation of the *eag* gene leads to enhanced neuronal excitability (Ganetzky and Wu, 1983). In mammals, two isoforms of the EAG channel are known, exhibiting strongest expression in distinct areas of the brain (Ludwig et al., 1994; Occhiodoro et al., 1998; Saganich et al., 1999) or in the retina (Frings et al., 1998). These two isoforms, EAG1 and EAG2, share the typical regulation by extracellular Mg^{2+} and intracellular Ca^{2+} ions (Ludwig et al., 2000; Schönherr et al., 2002), but the structural basis of both forms of modulation is unknown. In principle, modulation could occur via an effect on the voltage sensor, gate, or sensor-gate coupling. To understand the mechanisms of switching between gating modes, we need detailed knowledge about the molecular events underlying voltage sensing and its coupling to gates in the pore.

The positively charged S4 segments of voltage-gated K^+ and Na^+ channels act as primary voltage sensors, moving across the transmembrane electric field in response to changes in membrane potential (Yang and Horn, 1995; Larsson et al., 1996; Mannuzzu et al., 1996; Yang et al., 1996; Yusaf et al., 1996; Baker et al., 1998; Wang et al., 1999) in a motion that involves rotation and which may be accompanied by an axial translation (Cha et al., 1999; Glauner et al., 1999). This motion generates the gating current via a displacement of basic residues through the electric field (Aggarwal and MacKinnon, 1996; Seoh et al., 1996; Starace et al., 1997; Starace and Bezanilla, 2001). Transmembrane segments S1, S2, and S3 are thought to wrap around S4 and to shield it from lipid, thus shaping the electric field across S4.

S4 motion is coupled to motions of at least two distinct gating structures in the pore domain (see Yellen, 1998, for review): an inner gate formed by the helices corresponding to the S6 segments in Shaker K^+ channels (Doyle et al., 1998; Perozo et al., 1999; Liu et al. 2001) and an external gate, involved in slow inactivation, which is located at the outer mouth of the pore (Liu et al., 1996; Baukrowitz and Yellen, 1996; Harris et al., 1998; Morais-Cabral et al., 2001). Interaction between S4 and the "turret" at the outer end of S5 has been proposed to couple the voltage sensing to a motion of the external gate (Gandhi et al., 2000; Larsson and Elinder, 2000; Loots and Isacoff, 2000; Elinder et al., 2001), and S4 rotation may twist S5 to open the internal gate (Glauner et al., 1999; Perozo et al., 1999).

How are the gates controlled, and how is gating regulated? Central to the original model of voltage-dependent gating by Hodgkin and Huxley (1952) is the idea that activation occurs in a series of transitions of several voltage sensors (now known to reside in four similar or identical subunits), which finally open the channel. Each transition follows an exponential time course upon change of membrane potential. During activation from a positive voltage, where all but one of the voltage sensors start off activated, channel opening follows the exponential activation step of that last sensor. In contrast, when starting at negative voltage, where all four voltage sensors must be activated, opening is delayed, since all of the sensors must be activated, and the rise in ionic

[3]Correspondence: eisacoff@socrates.berkeley.edu

current becomes sigmoidal. Hodgkin and Huxley used this sigmoidicity to estimate the minimal number of identical transitions that could account for K^+ channel gating, and this kind of analysis has been extended to Shaker channels (Zagotta et al., 1994).

EAG channels also open with increased sigmoidicity from more negative potentials, but the unusually large magnitude and Mg^{2+}-dependence of this behavior suggest that a distinct mechanism may be involved (Terlau et al., 1996; Schönherr et al., 1999; Tang et al., 2000). In principle, modulation of EAG channel opening by Mg^{2+} could occur via an effect on the voltage sensor or the activation gate or on the coupling between them. Recent work on *Drosophila* EAG attributed Mg^{2+} binding to a pair of acidic residues in S2 and S3 that are specific to channels in the EAG subfamily (Silverman et al., 2000). Since S2 and S3 interact with S4 (Papazian et al., 1995; Tiwari-Woodruff et al., 1997), this raises the possibility that Mg^{2+} alters EAG gating by altering S4 motion. This notion is supported by the observation that Mg^{2+} affects the gating current in *Drosophila* EAG (Tang et al., 2000). Indeed, a good quantitative description of EAG activation kinetics can be achieved using a kinetic model that adds a slow, Mg^{2+}-dependent gating step prior to the main closed to open transition (Schönherr et al., 1999). However, in *Drosophila* EAG the effect of Mg^{2+} on gating current kinetics is much smaller than on opening kinetics (Tang et al., 2000), suggesting that the primary action of Mg^{2+} may not be on S4 but, instead, that Mg^{2+} may act on either the gate or the coupling mechanism.

To determine whether Mg^{2+} affects S4 motion in EAG and to define the extent to which modulation of the voltage-sensing steps can account for the modulation of gating, we applied three types of analysis to the bovine EAG1 channel (bEAG1): (1) perturbation mapping of protein interaction sites on S4 that are important for slow gating mode stability; (2) accessibility mapping to define the voltage and Mg^{2+} dependence of S4 topology; (3) fluorescence determination of motions of S4 relative to its environment. We define the voltage-dependent topology of bEAG1's S4 and find that side chain alterations at sites buried in the gating canal at rest selectively perturb the slow gating mode. In addition, we obtain quantitative evidence that voltage- and Mg^{2+}-dependent slowing of channel opening can be accounted for by a retardation of S4 motion in individual subunits. The accessibility and fluorescence measurements suggest that there are two kinds of protein motion in the voltage-sensor domain: (1) a motion of S4 that carries gating charge across the membrane and (2) a rearrangement of S2/S3 that depends on Mg^{2+} binding and S4 conformation. The second rearrangement is proposed to regulate the first: Mg^{2+} binding locks the canal in a narrow conformation, which locks down on the narrow outer end of S4 and prevents its outward motion, thereby slowing activation and, consequently, slowing channel opening.

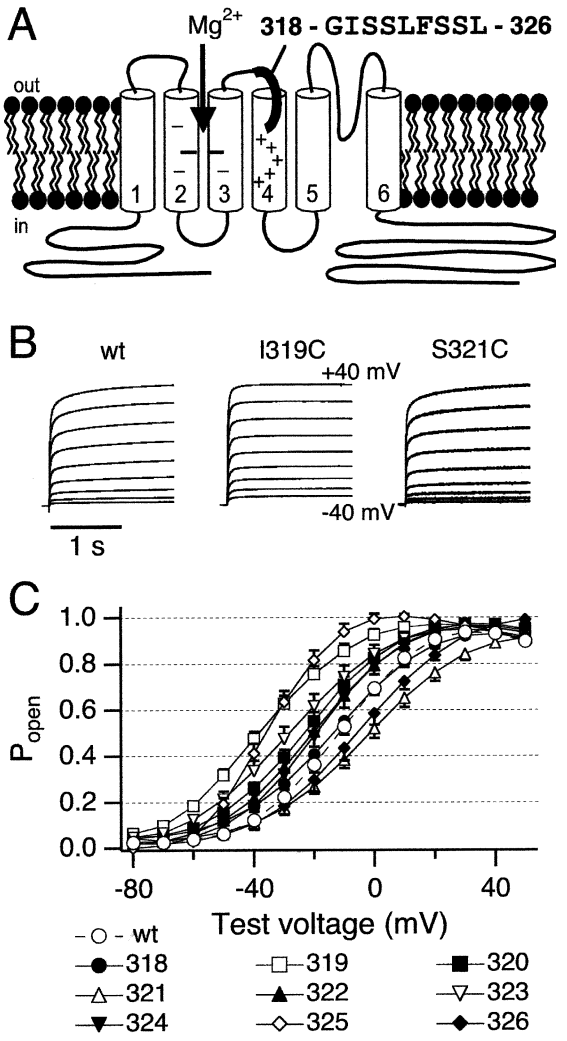

Figure 1. Perturbation of Mg-*Independent* Fast Gating by Cysteine Substitution

(A) Schematic topology model of a bEAG1 α subunit. The indicated amino acid residues 318–326 were individually replaced by cysteine, ending just before the first basic residue in S4. Conserved acidic residues in S2 and S3 thought to interact electrostatically with basic residues in S4 are shown as small minus signs, and acidic residues specific to EAG and thought to form the externally accessible Mg^{2+} binding site that modulates activation are shown as large minus signs.

(B) Activation kinetics of wild-type (wt) and of cysteine mutants with largest negative (I319C) and largest positive (S321C) shifts in *G-V*. Currents in the absence of external Mg^{2+} were measured in response to a series of voltage steps from a holding potential of −100mV.

(C) Normalized *G-V* relations of wt and cysteine mutants from traces as in (B), fit with single Boltzmann curves. Conductance was calculated after fitting the currents at the end of the steps as a function of voltage according to equation 2 with n = 1. The strongest negative and positive deviations in V_h relative to wt (−11.8mV ± 2.0mV) were −35.8mV ± 2.3mV for I319C and S321C and −2.1mV ± 2.9mV for S321C, respectively (n = 8–12).

Results

Perturbation of Fast and Slow Gating by Cysteine Mutations at the Outer End of S4

We replaced individual residues in the extracellular end of the bEAG1 S4 segment with cysteine, starting at G318 and ending with L326, the residue preceding the first positive charge in S4 (Figure 1A). Residues upstream of G318 were not tested, as a splice variant with a 27 amino acid insertion at this position undergoes slow gating not markedly different from bEAG1 (Frings et al., 1998). As

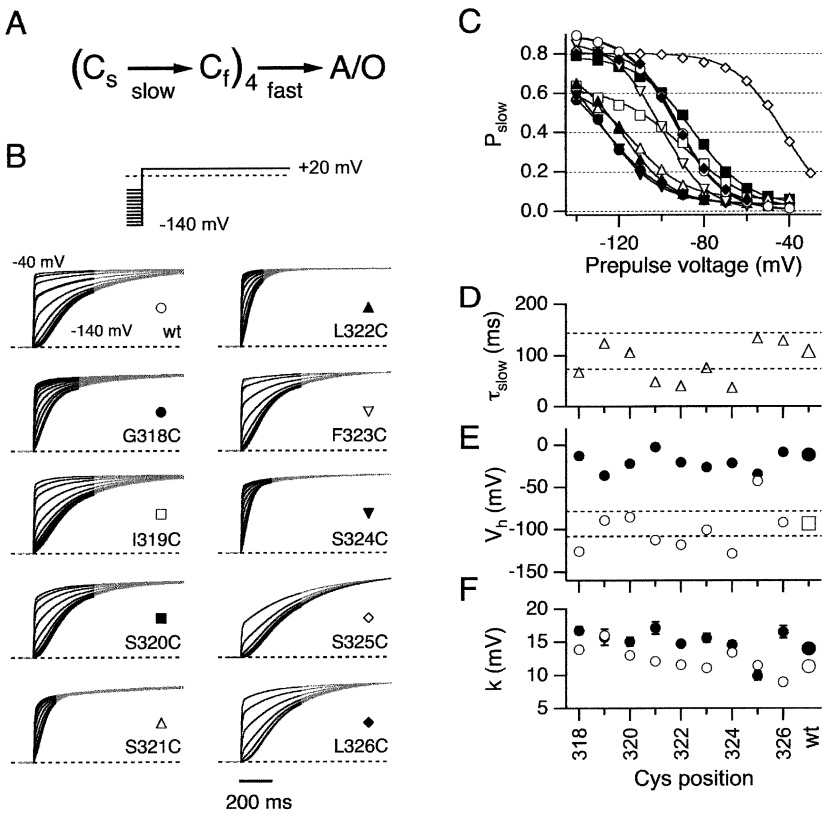

Figure 2. Perturbation of Mg-*Dependent* Slow Gating by Cysteine Substitution

(A) Gating scheme applied for analysis of bEAG channel activation.

(B) Current responses from oocytes expressing wt and the indicated mutants were recorded in 5 mM Mg^{2+}. Five-second prepulses ranging from −140mV to −40mV were applied before a depolarizing step to +20mV. Traces are averages from 5 to 15 individual oocytes (gray). Superimposed are fits (black) according to equation 1 (see Experimental Procedures). Note that cysteine substitution reduces prepulse slowing of activation at some sites (318, 321, 322, 324) and shifts prepulse voltage dependence at another (325).

(C) Probabilities of individual channel subunits to reside in the slow closed state (P_{slow}) were derived from the fits to average currents in (B) and are plotted *versus* prepulse potential. The curves are single Boltzmann fits to the data points (same symbols as in [B]).

(D) The time constant (τ_{slow}) for slow activation after a 5 s prepulse to −140mV, derived from the fits in (B) plotted for the wild-type (large symbol) and the mutants.

(E) The midpoint (V_h) of the *G-V* (closed circles) and the P_{slow}-*V* relation (open circles) for the mutants (small symbols) and wild-type (large symbols). Values are from the fits in Figures 1C and 2C. Note the absence of correlation between the midpoints of the *G-V* and P_{slow}-*V*.

(D and E) τ_{slow} and P_{slow} values falling between the dashed lines that bracket the wild-type are defined as low impact, while those beyond the dashed lines are defined as high impact (318, 321, 322, 324, and 325) and modeled on an α helix in Figure 8.

(F) Slope factors (k) of the Boltzmann fits to the *G-V* (closed circles) and P_{slow}-*V* data (open circles).

expected for the S4 region, the tested mutations influenced the voltage dependence of channel opening (*G-V*) (Figures 1B and 1C), but the effects (shifts of +10mV to −24mV) were milder than those reported for deeper uncharged sites in both Shaker and Kv2.1 channels (Lopez et al., 1991; Li-Smerin et al., 2000). These bEAG1 cysteine mutations had little or no effect on the kinetics of Mg^{2+}-*independent* fast activation (e.g., Figure 1B) as far as can be judged with the two-electrode voltage clamp method applied to *Xenopus* oocytes.

In contrast, some of the mutations had strong effects on Mg^{2+}-*dependent* slow gating (Figure 2). All of the mutants retained sufficient Mg^{2+}-dependent slow gating (Figure 2B), permitting analysis of the early, rate-limiting steps of activation. As shown previously for wild-type channels in 5 mM Mg^{2+} (Schönherr et al., 1999), more negative prepulse potentials resulted in slower and more sigmoidal turning-on of the ionic current (Figure 2B). To describe the activation kinetics quantitatively, we used an approach described previously (Schönherr et al., 1999), assuming that channel subunits activate with either fast kinetics from depolarizing prepulses or with slow kinetics from hyperpolarizing prepulses (Figures 2A and 2B) and attributing to a subunit the probability, P_{slow}, that it resides in the state from which activation is slow. Based on a binomial distribution of channel subunits between fast and slow activation modes (equation 1, Experimental Procedures), we were able to describe the activation of the ionic current, including the early sigmoidal rising phase. Fits with this model faithfully described the measured current (Figure 2B), and they provided values for three free parameters: P_{slow} and the time constants for slow (τ_{slow}) and fast activation (τ_{fast}). The component representing fast activation (τ_{fast}), however, was too close to the resolution limit of the voltage clamp to be analyzed systematically.

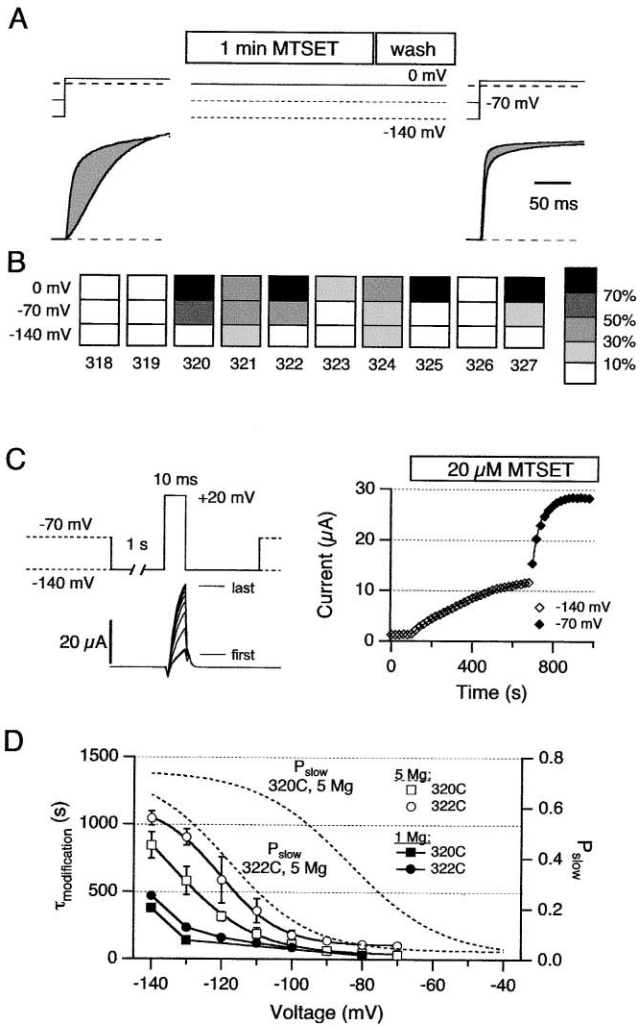

Figure 3. Voltage-Dependent Accessibility at the Outer End of S4

(A) Prepulse-dependent current responses of L322C in 5 mM Mg^{2+} before (left) and after (right) MTSET perfusion (pulse protocol on top). MTSET (20 μM) was applied for 1 min at a holding potential of 0mV. MTSET modified the site, yielding rapidly activating channels with reduced prepulse dependence.

(B) The indicated cysteine mutants were analyzed for MTSET sensitivity using the same protocol as in (A). The relative MTSET effect on the activation kinetics was determined as the ratio of the integrals between current traces from −70mV and −140mV (gray areas in [A]). For each mutant, MTSET modification was assayed at three different holding potentials (−140mV, −70mV, and 0mV) in individual oocytes ($n \geq 3$). Relative modification indicated by shading according to the scaling (right), with white indicating changes of <10%.

(C) MTSET modification of L322C during repetitive pulsing. The cell was held at −70mV, and every 20 s slow activation was assayed by 1 s prepulses to −140mV, followed by a short (10 ms) test pulse to +20mV. After five repetitive pulses in control bath solution, continuous perfusion with MTSET was initiated. The resulting modification accelerated the activation kinetics, leading to increased currents during the 10 ms test pulse (left). Peak currents in the 10 ms test pulses are plotted as a function of time (right). The oocyte was initially held at −140mV (open symbols) and then at −70mV (filled symbols). The bar indicates MTSET application. Single exponential fits to the data points are superimposed.

(D) Voltage-dependent modification of mutants 320C and 322C in 5 mM (open) and 1 mM Mg^{2+} (filled symbols). The time constants for MTSET modification were derived from single exponential fits to currents measured from experiments as in (C), using one holding voltage per oocyte and modifying to completion. Values from experiments in 1 mM Mg^{2+} are connected by straight lines; single Boltzmann functions are fitted to data points from experiments in 5 mM Mg^{2+} ($n \geq 3$). Note the depolarized shift in accessibility at both sites in higher [Mg^{2+}]. The dashed curves indicate the P_{slow}-V relationships of Figure 2C.

With these parameters in hand, we were able to quantify the extent to which the cysteine mutations perturbed Mg^{2+}-dependent slow gating. We found that the voltage dependence of P_{slow} (P_{slow}-V) was strongly shifted (by 20mV–50mV) at some positions—318, 321, 322, 324, and 325—but only weakly shifted (by 0mV–10mV) at several other positions—319, 320, 323, and 326 (Figures 2C and 2E). With the exception of 325, all sites that had a high impact on the voltage dependence of P_{slow} were also strongly perturbed in τ_{slow} kinetics, showing a marked reduction in the influence of hyperpolarizing prepulses, both on slowing and sigmoidicity of activation (Figures 2B and 2D). Assuming a continuous α-helical structure of S4, it is remarkable how all high-impact sites are concentrated on one face of the putative helix, while residues with low impact on P_{slow}-V are found on the opposite side (Figure 8B).

Not only were the effects on the G-V small compared to the high-impact effects on the P_{slow}-V, but there was no correlation in either the direction or magnitude of these shifts (Figure 2E). This suggests that distinct conformations of the voltage-sensing domain dominate P_{slow} and the open states. In contrast to the influence on P_{slow}-V, the impact of individual residues on G-V does not show a defined orientation in a helical projection of S4. We next probed the conformations of the voltage-sensor domain in an accessibility scan of the S4 region at different voltages.

Voltage Dependence of Accessibility to Introduced Cysteine

We assayed the accessibility of each of the substituted cysteines by exposure to the charged methanethiosulfonate MTSET in the external solution, using a functional report of cysteine conjugation. The traces in Figure 3A show how conjugation with MTSET (20 μM for 1 min) of a cysteine at site 322 modified gating: strongly accelerating slow gating and modestly accelerating fast gating. A similar effect (data not shown) was observed when the channels were exposed to the negatively charged MTSES (100 μM for 1 min). Wild-type channels did not respond to either MTSET or MTSES (data not shown). This approach permitted us to gauge the degree of impact on slow activation kinetics. To assay the state de-

pendence of accessibility, we applied MTSET for a constant period of time (1 min) at three different voltages, i.e., holding the channels in closed states with high (−140mV) or low (−70mV) P_{slow} values or else holding the channels open at 0mV. Out of sites 318 to 327, MTSET exposure at 0mV affected slow gating at 320–325 and 327 (Figure 3B). The mutant K327C was included here for better comparison to accessibility data from Shaker channels. This mutation strongly disturbed channel gating. Ionic currents did not reach steady state during 10 s test pulses, and activation kinetics varied for individual oocytes (data not shown). However, conjugation with MTSET could be judged from a strong acceleration of activation kinetics (data not shown). The degree of modification was higher at all of the affected sites at more depolarized voltages (Figure 3B). Although there was no effect on slow gating at 318 and 319, shifts in the *G-V*s indicated that conjugation did take place, even when MTSET exposure was performed at a holding potential of −70mV (V_h shifted from −12.9mV ± 2mV to +2.2mV ± 4.0mV, n = 6 at 318, and from −35.8mV ± 2.3mV to −57.9mV ± 2.3mV, n = 8 at 319). There was no discernable impact of MTSET on mutant 326C.

The results indicate that residues 318, 319, 321, and 324 are always accessible externally and that external access to 320, 322, 323, 325, and 327 is voltage dependent, yielding more complete conjugation at depolarized voltage. Residue 326 is either never exposed externally or has little influence on gating. The voltage dependence of accessibility of S4 of bEAG1 is consistent with a substantial outward motion of S4 from the gating canal, as found in Na^+ channels and Shaker K^+ channels (Yang and Horn, 1995; Larsson et al., 1996; Mannuzzu et al., 1996; Yang et al., 1996; Yusaf et al., 1996; Baker et al., 1998; Wang et al., 1999). We can add that MTSET conjugation of 318 and 319 selectively affects fast gating, whereas conjugation at 320–325 affects slow gating, arguing that the slow gating mode is selectively perturbed by the introduction of bulk or charge at residues that are buried in the canal at rest.

Relationship between S4 Accessibility and the Transition between Fast and Slow Gating Modes

Does the observed voltage-dependent change in S4 exposure in bEAG1 channels simply reflect activation/deactivation, as thought to occur in Shaker channels, or could entry and exit from the slow gating mode also alter the conformation of S4 or of the canal that surrounds it? We compared the voltage dependencies of accessibility and P_{slow}. The voltage dependence of accessibility varied between the different cysteine mutants (Figure 3B). The crude analysis in Figure 3B together with Figures 2C and 2E shows parallel shifts of P_{slow}-*V* and accessibility for at least three sites—321, 324, and 325. In accord with hyperpolarized shifts of P_{slow}-*V* for the two mutants 321C and 324C, these sites could not be completely protected from modification at the most negative holding potential that we were able to use (−140mV). In turn, the depolarized voltage dependence of 325C paralleled a depolarized shift in accessibility. However, these parallels broke down for residue 323C, where the voltage dependencies of accessibility and P_{slow} were shifted in opposite directions (Figures 2C and 2E). For two sites that appeared to have similar voltage dependencies of accessibility (320, 322), we examined the voltage dependence of MTSET access more quantitatively. Oocytes in 5 mM Mg^{2+} were clamped at a range of holding potentials, and modification was assayed in 20 s intervals by a short (10 ms) test pulse to +20mV, preceded by a step to −140mV for 1 s to induce slow gating (Figure 3C, top left). This protocol was repeated continuously, and MTSET perfusion was started after five baseline pulses. Due to their slow activation, unmodified channels showed almost no current during the brief test pulse (Figure 3C, bottom left), while modification led to increased current amplitudes. Figure 3C (right) illustrates the rise of current over time and the increased modification rate at more depolarized holding potentials, when the holding potential was switched partway through modification. Modification-voltage curves were based on modification to completion at only one holding voltage per oocyte, and the time course of modification was fit with a single exponential to determine the time constant of modification (Figure 3C). We found that accessibility at both 320C and 322C depended on extracellular Mg^{2+}, with 5 mM Mg^{2+} shifting the voltage dependence of accessibility to the right (Figure 3D), as found earlier for gating charge movement in *Drosophila* EAG (Tang et al., 2000). For 322C, the voltage dependence of modification closely followed that of P_{slow}, determined for nonmodified 322C channels under the same conditions (Figure 3D, dashed line). In contrast, the modification-voltage curve for 320C was far to the left of the P_{slow}-*V* curve.

In summary, S4 accessibility at some sites (321, 322, 324, and 325) appears to follow P_{slow}, but at other sites (320 and 323), it depends on another voltage-dependent step. It is noteworthy that the four sites whose exposure follows P_{slow} are all sites of high impact on slow gating, while the two sites that do not are low-impact sites (Figure 8B).

S4 Fluorescence Tracks Both Fast and Mg^{2+}-Dependent Slow Activation Steps

We employed voltage clamp fluorometry (VCF) to obtain a real-time report of the protein motions underlying activation and deactivation, as well as entry and exit from the slow gating mode. Sites 318 to 326 were labeled with 5′ TMRM, and VCF experiments were performed. From four sites (320, 323, 325, 326) we did not obtain significant fluorescence signals. At 322C and 324C, where the cysteine mutation had a high impact on slow gating and where MTSET conjugation modified slow gating further, TMRM virtually eliminated slow gating, leaving only fast gating that was tracked by a fast fluorescence change (ΔF) (data not shown). In contrast, more superficial sites 318C, 319C, and 321C were successfully labeled, and TMRM did not eliminate slow gating, enabling us to carry out the analysis of state-dependent fluorescence (Figures 4A–4D). We examined the reports of local protein motion around these sites during the responses of channels to depolarizing test pulses that opened the channels. A short test pulse from the holding potential was followed by a strong hyperpolarization and then a second longer test pulse. This was

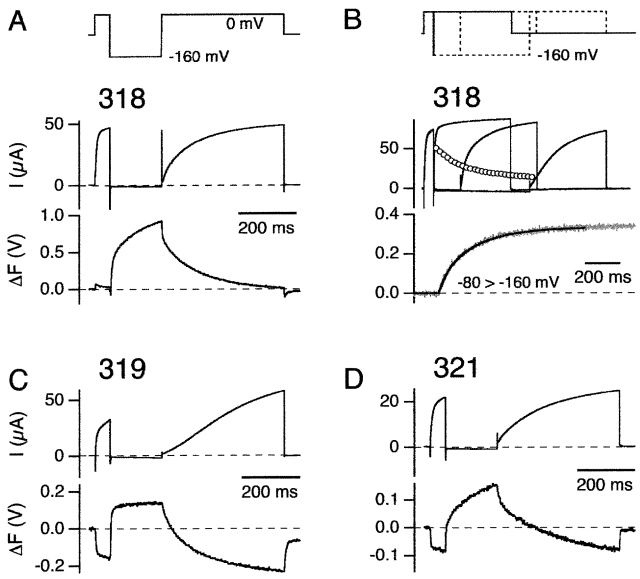

Figure 4. Fluorescence at Sites of High and Low Impact on Slow Gating: Tracking Opening and Slow Gating

Ionic current responses (upper traces) and fluorescence changes (lower traces) of TMRM attached at the indicated cysteine positions. (A, C, and D) Current and fluorescence responses to depolarizing pulses to 0mV, first from the holding voltage of −80mV and then following a 200 ms step to −160mV, are shown in 5 mM Mg^{2+} solutions. Note that the initial depolarization from −80mV elicits fast opening and ΔF and that both are slowed by the hyperpolarization to −160mV. Note also that a slow ΔF during the hyperpolarization to −160mV is evident for 318C and 321C but not for 319C. (B) Kinetic comparison of the slow ΔF in 318C with the onset of slow gating. Voltage steps (top) from a holding potential of −80mV to 0mV to open channels were followed by hyperpolarizing steps to −160mV for variable duration, followed by steps to 0mV to open channels for a second time. The ionic current responses were slowed and increased in sigmoidicity in proportion to the duration of the prepulse hyperpolarization. Time course of entry into the slow gating mode during the hyperpolarizing prepulse was determined from the progressive decline with longer prepulses in normalized current amplitude 25 ms after the start of the second step to 0mV. Entry into the slow gating mode was described by a single exponential with a time constant of 185 ± 18 ms (n = 6). The fluorescence report of local protein motion at 318 during a hyperpolarizing pulse from −80mV to −160mV (below) was well fit by a single exponential with a time constant of 214 ± 2 ms (n = 5).

done in the presence of external Mg^{2+} to promote slow gating. The fluorescence response (ΔF) at 318, 319, and 321 varied in direction and relative magnitude. All three had a fast ΔF and opened quickly in response to the short test pulse from a holding potential of −80mV. Prepulse hyperpolarization slowed opening and slowed the ΔF in parallel (Figures 4A, 4C, and 4D). This suggests that voltage modulates the rate of opening by regulating the rate of S4 motion.

While fluorescence kinetics from all three mutants were similar during depolarizing steps, the most obvious differences concerned entry into the slow gating mode. Note in Figure 4 that 318 and 321 channels, which had high impact on P_{slow} (Figure 2E), show a slow change in ΔF *during* the hyperpolarization step, at the time that channels entered the slow gating mode (Figures 4A and 4D). In contrast, fluorescence from the intervening low-impact site 319 did not track a slow step *during* hyperpolarization (Figure 4C).

Does this mean that this ΔF from high-impact sites tracks *entry* into the slow gating mode? For 318-TMRM channels, we determined the rate of entry into the slow gating mode from changes in the rate of channel opening, following hyperpolarizing prepulses (to −160mV) of increased duration (starting from 5 ms and incrementing by 23 ms to a maximum of 580 ms). Increasing prepulse duration slowed channel opening and increased the sigmoidicity of the rise of the current (Figure 4B). The fraction of channels in the slow gating mode was determined from the current amplitude 25 ms after the start of the depolarizing test pulse. The fraction in the slow gating mode was plotted against the duration of the prepulse. This time course was fit by a single exponential with a time constant of 185 ± 18 ms (n = 6) (Figure 4B). The parallel slow increase in fluorescence during the prepulses was fit by a single exponential, with a time constant of 214 ± 2 ms (n = 5). This similarity in time constants argues that 318-TMRM fluorescence tracks *entry* into the slow gating mode.

In summary, fluorescence at high-impact sites appears to track *entry* into the slow gating state, while *exit* from the slow gating mode is tracked by fluorescence at both high- and low-impact sites. It should be noted that the lack of a slow fluorescence component in 319C channels during entry into the slow state is not caused by faster entry kinetics. In experiments with 319C analogous to those shown in Figure 4B, the time constant for the slowing of current kinetics was 113 ± 6 ms, and 42 ± 4 ms for fluorescence kinetics (n = 8) (data not shown).

Transitions between Closed States and the Steady-State Voltage Dependence of Voltage-Sensor Domain Rearrangements

If the prepulse-dependent slowing of fluorescence kinetics seen in Figure 4 is correlated to slow gating, we should also find this ΔF to be modulated by Mg^{2+}. For further analysis, we focused on high-impact site 318 and low-impact site 319, as they routinely gave large ΔFs. We examined fluorescence responses to hyperpolarizing steps from −80mV, a voltage where channels are closed and at least half of them are in the fast gating mode. For 318 channels, the kinetics of ΔF were clearly slowed by Mg^{2+}, both during entry (hyperpolarization) and exit (repolarization) from the slow state (Figure 5A). In contrast, 319 channels were slowed by Mg^{2+} during repolarization (e.g., from −190mV) and depolarization (+30mV) but not during hyperpolarizing steps (Figure 5C).

The steady-state fluorescence-voltage relation (ΔF-*V*)

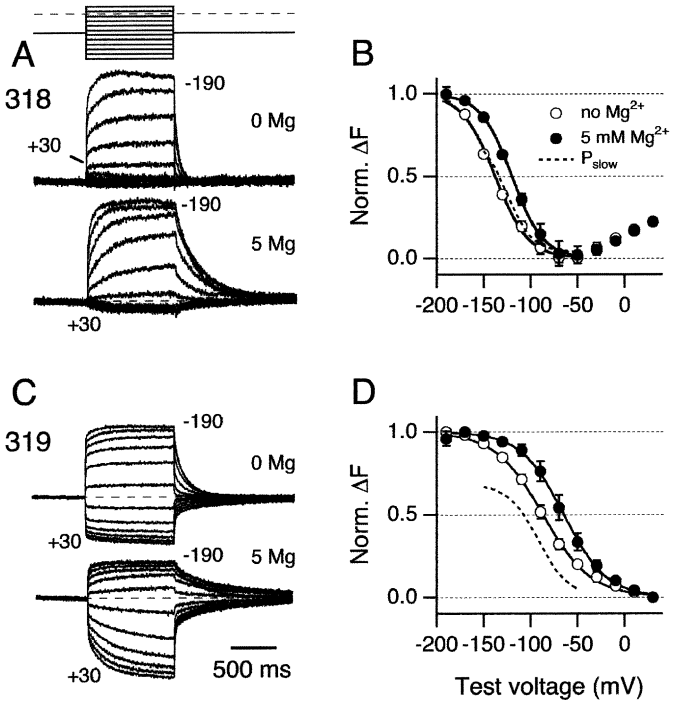

Figure 5. Voltage Dependence of Fluorescence at Sites 318 and 319

(A and C) Normalized fluorescence responses to 1 s steps from a holding potential of −100mV to voltages ranging from −190mV to +30mV, in 20mV increments in 0 mM (upper) and in 5 mM Mg^{2+}. Note that at both sites the fluorescence *recovery* from P_{slow} upon return from a hyperpolarization to −80mV is slowed by Mg^{2+}. Moreover, as seen for mutant 318C, Mg^{2+} also slows *entry* into P_{slow} during the hyperpolarizing step.

(B and D) Normalized ΔF-V relations (values measured at the end of the step) reveal a shift of ~20mV to the right in 5 mM Mg^{2+}. Continuous curves are Boltzmann fits for 318 (0 Mg^{2+}: V_h = −137.9mV ± 1.2mV, k = −17.5mV ± 1.1mV; 5 mM Mg^{2+}: V_h = −120.2mV ± 0.5mV, k = −16.6mV ± 0.5mV; n = 6) and 319 (0 Mg^{2+}: V_h = −87.1mV ± 0.9mV, k = −25.6mV ± 0.8mV; 5 mM Mg^{2+}: V_h = −64.8mV ± 0.8mV, k = −22.8mV ± 0.7mV; n = 7). For comparison, the P_{slow}-V relations of the unlabeled mutants in 5 mM Mg^{2+} are shown as dashed curves (from Figure 2C). Note the similarity between ΔF-V and P_{slow}-V at site 318 and the difference between these relations at 319.

at 318 had minimal brightness at about −60mV. Depolarization increased fluorescence modestly, and hyperpolarization increased it considerably. This flip in direction of ΔF indicates that 318-TMRM reports on at least two different protein motions in the voltage-sensor domain: an "early" step at hyperpolarized potentials and a "late" step at depolarized potentials that continues to very depolarized potentials. There was also a close agreement between the voltage dependencies of the early fluorescence component and that of P_{slow} (Figure 5B). Mg^{2+} increased the stability of the slow gating mode conformation registered by 318-TMRM, shifting its voltage dependence to the right by ~20mV (Figure 5B). In contrast, the late fluorescence component of 318-TMRM was not shifted by Mg^{2+}, consistent with the relative insensitivity of the G-V to Mg^{2+} (Terlau et al., 1996; Tang et al., 2000).

At 319, fluorescence declined steadily with depolarization throughout the voltage range, and the voltage dependence was well described by a single Boltzmann function (Figure 5D). In contrast to the high-impact site 318, where the ΔF-V in 5 mM Mg^{2+} was similar to the P_{slow}-V (Figure 5B), at low-impact site 319, the ΔF-V differed from the P_{slow}-V. 319-TMRM fluorescence reported conformational change(s) occurring at more positive potentials. The voltage dependence of this conformation change was also shifted to the right in 5 mM Mg^{2+} by ~20mV. These motions likely reflect the charge-carrying transmembrane motion of S4. Although the ΔF-V of 319-TMRM does not follow the P_{slow}-V and entry into the slow gating mode is not reported by 319-TMRM, the fluorescence kinetics upon depolarization are rate limited by the exit from the slow gating mode. This was also seen for steps positive enough to open the channels following a hyperpolarizing prepulse (Figure 4C). Here we see that partial activation upon return from hyperpolarized potentials to −80mV is also slowed by Mg^{2+} (Figure 5C).

The observed behavior suggests that upon depolarization from hyperpolarized potentials in external Mg^{2+} a slow rate-limiting exit from the slow gating mode is followed by fast S4 activation motion, which is followed, in turn, by channel opening.

Quantitative Analysis of Channel Opening and S4 Fluorescence Kinetics

Given the voltage dependencies of ΔF for channels labeled at 318 and 319, it is tempting to assign the ΔF from 319 mainly to the late opening step of S4, while in the biphasic ΔF-V relationship of 318 only the small component at high voltages could potentially reflect this late step. If this assumption is correct, one should find a simple quantitative description of both current and fluorescence signals for both mutants.

We analyzed current (Figure 6E) and fluorescence (Figure 6F) signals from 319 in response to voltage steps ranging from −170mV to +50mV in 5 mM Mg^{2+}. The ΔF-V relation was well fit by a single Boltzmann function with a V_h value of −57.2mV and a slope factor of 15.8mV (Figure 6G). Using these values from the fluorescence data in a constrained Goldman-Hodgkin-Katz fit (equation 2) in which the exponent was set to n = 4, thus only leaving the conductance as a free parameter, resulted in an excellent description of the I-V relation (curve through open circles in Figure 6G). This confirms that the protein motion underlying the fluorescence signal in mutant 319C is tightly coupled to channel opening.

Although ΔF of 319 appears to report the late movement of S4, the tight coupling of channel opening to the slow gating process should lead to fluorescence signals which track τ_{slow} derived from the analysis of ionic currents. As fluorescence changes directly report move-

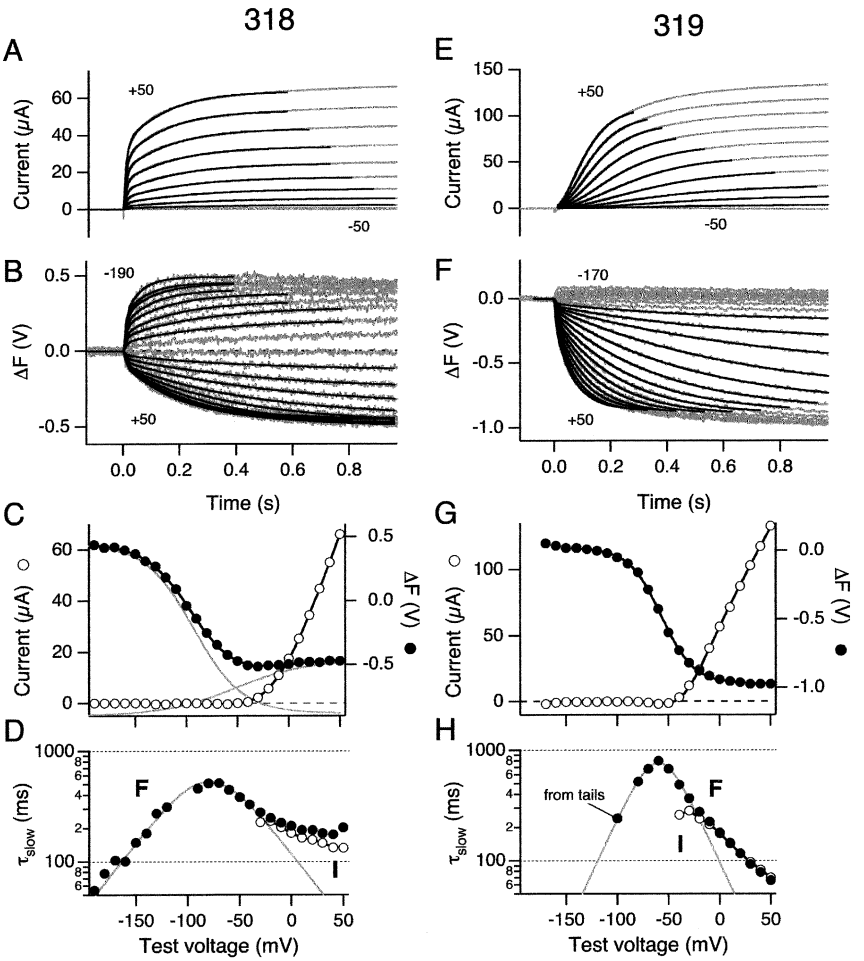

Figure 6. Quantitative Description of *I-V* and ΔF-*V* for Sites 318 and 319

(A–D) Data for 318-TMRM; (E–H) data for 319-TMRM in 5 mM Mg^{2+}. (A, B, E, and F) Current (A and E) and fluorescence (B and F) responses (gray) to voltage steps in the indicated range from a holding potential of −100mV. Black curves are fits according to equation 1 for the current (A and E) and double exponential fits for the fluorescence (B and F). (C and G) The normalized ΔF (closed circles) and the current (open circles) at the end of the test pulse plotted *versus* test voltage. For mutant 318, the ΔF values are described by a two-component Boltzmann fit; the individual components are indicated as gray curves. For mutant 319C, ΔF data are described by a single Boltzmann function. The *I-V* relation for mutant 319C was fit according to a Goldman-Hodgkin-Katz formalism, using the V_h value and slope factor obtained from the Boltzmann fit to the ΔF-*V* curve ($V_h = -57.2$mV; $k = 15.8$mV), assuming four independent gating units, i.e., n = 4 in equation 2. For mutant 318, this fit was performed with the second component of the Boltzmann function ($V_{h1} = -92.6$mV; $k_1 = 23.6$mV; $V_{h2} = -51.9$mV; $k_2 = 35.0$mV). (D and H) τ_{slow} values from fits of current in (A and E) (open symbols) and fluorescence in (B and F) (closed symbols). The data point "from tails" in (H) was obtained from fluorescence relaxations to −100mV following depolarization. The bell-shaped curves represent the expected voltage dependence of a simple one-step reaction, fitted to the fluorescence kinetics up to −20mV.

ments of individual subunits, independent of the final opening step, it should be possible to describe slow and fast gating steps by double exponential functions. Indeed, satisfactory fits of the fluorescence responses during the test pulse were obtained by this approach (Figure 6F). As hypothesized, the time constants of the slow fluorescence component (Figure 6H, closed circles) are quite similar to τ_{slow} values (Figure 6H, open circles) obtained from ionic currents using the previously applied model (equation 1, black curves in Figure 6E).

Assuming that the slow fluorescence change is associated with a single voltage-dependent step obeying Eyring's law, the voltage dependence of this corresponding time constant was described by the bell-shaped curve $\tau(V) = 1/(\alpha(V) + \beta(V))$, with voltage-dependent forward [$\alpha = \alpha_0 \exp(-(V - V_0)/sl)$] and backward [$\beta = \alpha_0 \exp((V - V_0)/sl)$] rate constants (Figure 6H, gray curve). The close match between data and function in the voltage range where channels have not yet opened indicates that the slow fluorescence change is mainly determined by a single rate-limiting gating transition. At more depolarized potentials, further transitions take place which lead to channel opening. As expected, here the data points deviate from the prediction for a simple one-step reaction (Figure 6H).

The analogous analysis as described for 319 was performed for 318 (Figures 6A–6D), but the ΔF-*V* relation was fit by a two-component Boltzmann function; the gray curves in Figure 6C indicate the individual components. Only values from the smaller, second fluorescence component were used in the constrained Goldman-Hodgkin-Katz fit to current data, yielding a good

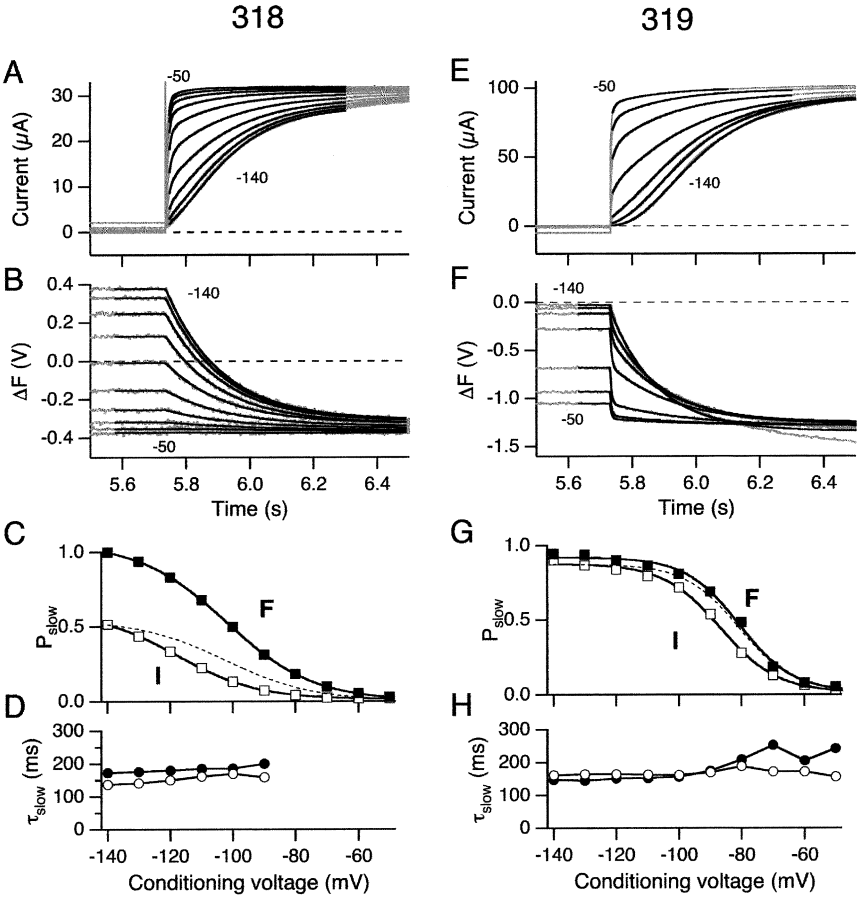

Figure 7. Prepulse Dependence of Current and Fluorescence Kinetics

(A–D) Data for 318-TMRM; (E–H) data for 319-TMRM in 5 mM Mg^{2+}. Five-second prepulses (−140mV to −50mV) were applied, followed by a constant test pulse to 0mV. (A and E) Current responses to this pulse protocol, mainly showing the depolarization phase. (B and F) Fluorescence recorded during the same experiments. Fluorescence at the holding potential (−100mV) was set to 0. Fits of the current data according to equation 1 (A and E) and of the fluorescence data using a single (B) or double exponential (F) are superimposed in black to the data (gray). (D and H) The time constants for the slow components in current (open circles) and fluorescence (closed circles) are plotted *versus* the prepulse voltages and are connected by straight lines. (C and G) The probabilities for slow gating, derived from the fits in (A) and (E) are plotted versus prepulse potential (open squares). In comparison, the relative amplitude of the slow fluorescence component is plotted (filled squares). Both relations were fitted to single Boltzmann functions, yielding V_h values for current and fluorescence: mutant 318C, −119.4mV and −102.1mV; mutant 319C, −86.4mV and −80.8mV, respectively. The dashed curves indicate the normalized fluorescence fits, scaled to the maximally obtained P_{slow} values. Note that while the fraction of channels with slow fluorescence increases with increased prepulse hyperpolarization, the slow fluorescence time constants are relatively constant. Note also that 318-TMRM fluorescence is dominated by slow exit from the slow gating mode, while 319-TMRM fluorescence switches from fast to slow as channels switch from fast to slow gating modes.

description (curve through open circles in Figure 6C). Analogous to 319, the kinetics of fluorescence data in the negative voltage range could be well described as a simple one-step transition (Figure 6D); they also deviated from this simple scheme at potentials where additional conformational changes, as the late S4 step, take place. The close match of τ_{slow} values derived from current data according to the binomial distribution model (equation 1, open circles in Figure 6D) and from fluorescence data according to a double-exponential fit (filled circles in Figure 6D) indicates the usefulness of this simple quantitative description.

Fluorescence at 318 and 319 Quantitatively Describes Prepulse Dependence of Activation

The model-dependent analysis of ionic currents from different prepulse potentials (equation 1, Figure 2B) yields data on the occupancy of the slow closed state as well as the time constant for exit from this state (τ_{slow}). As we made the assumption that a major fluorescence component of 318 channels directly reports exit from this slow state, we have to demand a close quantitative correlation between fluorescence in such experiments and the model-derived data from ionic currents. Our model assumes that the late S4 step is serially connected to the transition between the closed states. Thus, kinetics of fluorescence from 319 channels, although reporting the late S4 motion, should match closely to the kinetics of prepulse-dependent ionic currents.

Figures 7E–7H show a detailed comparison of such prepulse dependencies for 319 channels in 5 mM Mg^{2+}. To reach a steady state between C_{slow} and C_{fast} states, long conditioning prepulses (5 s) were applied, ranging from −140mV to −50mV, and activation kinetics were

analyzed during the subsequent test pulse to 0mV. Clear fluorescence changes during prepulses ranging from −90mV to −50mV (Figure 7F) reported directly on the conformational changes of activation that previously could only be deduced from their effect on opening in response to the subsequent test pulse. Fluorescence signals during the test pulse could be well described by double exponential functions (Figure 7F), while currents were described by the binomial activation model (Figure 7E). Unlike the ΔF-V, which did not correlate to P_{slow} (Figure 5D), the proportion of slow ΔF during relaxation from the prepulse reflected the occupancy of the slow state. Figure 7G shows the close correlation between the voltage dependence of P_{slow} (determined from current) and relative amplitude of the slow fluorescence in 319C channels. In addition, the time constant of the slow ΔF and τ_{slow} (determined from the current) agreed over a wide voltage range (Figure 7H).

Using the same prepulse protocol as described for 319 (Figures 7E–7H), we analyzed current and fluorescence signals for 318 in 5 mM Mg^{2+} (Figures 7A–7D). The fluorescence at the test pulse potential of 0mV was dominated by a single exponential component (Figure 7B, compare with Figure 7F for 319). In contrast to 319 channels, which reported switching between fast and slow gating modes, for 318 channels the contribution of fast fluorescence to the total ΔF at 0mV was very small. While P_{slow} from current data indicated a maximum occupancy of the slow state of 50% in the tested voltage range (Figure 7C), ΔF did not inform about the distribution between states. However, the voltage dependencies of ΔF (normalized in Figure 7C) and of P_{slow} were characterized by similar V_h values (V_h (P_{slow}) = −117.8mV, V_h (ΔF) = −102.2mV). In addition, the time constants derived from the current and fluorescence recordings showed very close similarity (Figure 7D).

In summary, the quantitative comparison of current and fluorescence from 318 and 319 channels supports our assignment of the observed fluorescence signals to a slow activation step between closed states (318) and a fast activation step leading to channel opening (318 and 319).

Discussion

We have combined a fluorescence analysis of the dynamics of protein motion in the voltage-sensing domain of a K^+ channel with a steady-state accessibility analysis to define S4 transmembrane topology and a perturbation analysis to reveal S4's protein packing in the gating canal. Together, these analyses enabled us to explore the molecular basis for the regulation by Mg^{2+} and voltage of the gating kinetics of an EAG channel, and they serve to explain the earlier perturbation maps of Shaker and Kv2.1 channels. We describe below how our results led us to conclude that EAG channels alternate between slow and fast gating modes by independently switching the structures of the four voltage-sensing domains of the channel between slow and fast voltage-sensing modes. We propose that distinct parts of the voltage-sensor domain are responsible for mode switching and activation.

While activation—as in other K^+ channels—is correlated to the charge-carrying transmembrane movement of S4, switching between gating modes appears to involve a conformational change in the gating canal. Our accessibility analysis indicates that the portion of EAG's S4 that occupies the gating canal at rest is narrower than that which resides in the canal in the activated state. Sequence and accessibility alignment indicate that this is a common feature of K^+ channels, implying that their gating canals must widen for S4 to move outward. One aspect of diversity in the rates of activation may be due to differences in the stability of the narrow canal conformation. EAG channels were shown earlier to have a specialized Mg^{2+} coordination between EAG-specific acidic residues in S2 and S3 (Silverman et al., 2000), but the mechanism by which this acts to slow channel opening was not known. We now propose that cross-bridging of S2 and S3 via Mg^{2+} holds the gating canal in a narrow conformation and that for S4 to activate Mg^{2+} must first dissociate, permitting the canal to widen. This provides a molecular mechanism for the allosteric regulation of EAG opening by Mg^{2+}. We discuss the general implications of a gating canal rearrangement in the function of other channels.

Mapping the Slow Gating Perturbation on S4

Accessibility probing enabled us to determine a plausible alignment between the S4s of bEAG1 and Shaker (Figure 8A). In bEAG1, the outer border of the canal is defined by residue 320, as this is the first residue that showed higher accessbility to MTSET in the activated state. Comparison to the boundaries defined for Shaker (Larsson et al., 1996; Baker et al., 1998; Wang et al., 1999) supports an alignment in which bEAG1 is missing Shaker's first basic residue (so that the first basic residue in EAG, K327, corresponds to the second basic residue in Shaker, R365), putting it in the same category as Kv2, Kv4, and fly (but not mammalian) Kv3 channels, which are similar enough to Kv1 to permit alignment based on sequence (Li-Smerin and Swartz, 2001).

Perturbation analysis at the outer end of EAG's S4 revealed that sites which influence the stability of the slow gating mode are confined to one face of the S4 helix (Figure 8B). The high-impact sites are all exposed externally (and thus not involved in intimate protein interaction) in the activated state (Figure 8C). This implies that the perturbation of EAG *slow gating* occurs when S4 is in its resting conformation—a conclusion that is consistent with the dependence of slow gating on preceding hyperpolarization. The situation is exactly opposite for deeper S4 sites found earlier to perturb *opening* in Kv2.1 (Li-Smerin and Swartz, 2001). Those Kv2.1 sites are predicted, based on sequence alignment with Shaker (Figure 8A), to be accessible internally at rest (Figure 8C, left) and thus free of intimate protein contact. They will enter the canal in the activated state, explaining why their mutation perturbs opening.

Two More Threads Added to an S4 Helical Screw

The outer end of S4 in bEAG1 and a deeper segment in Kv2.1 both have low-impact faces, which likely face lipid. These low-impact stripes run together into one continuous stripe (Figure 8C, right) that spirals down

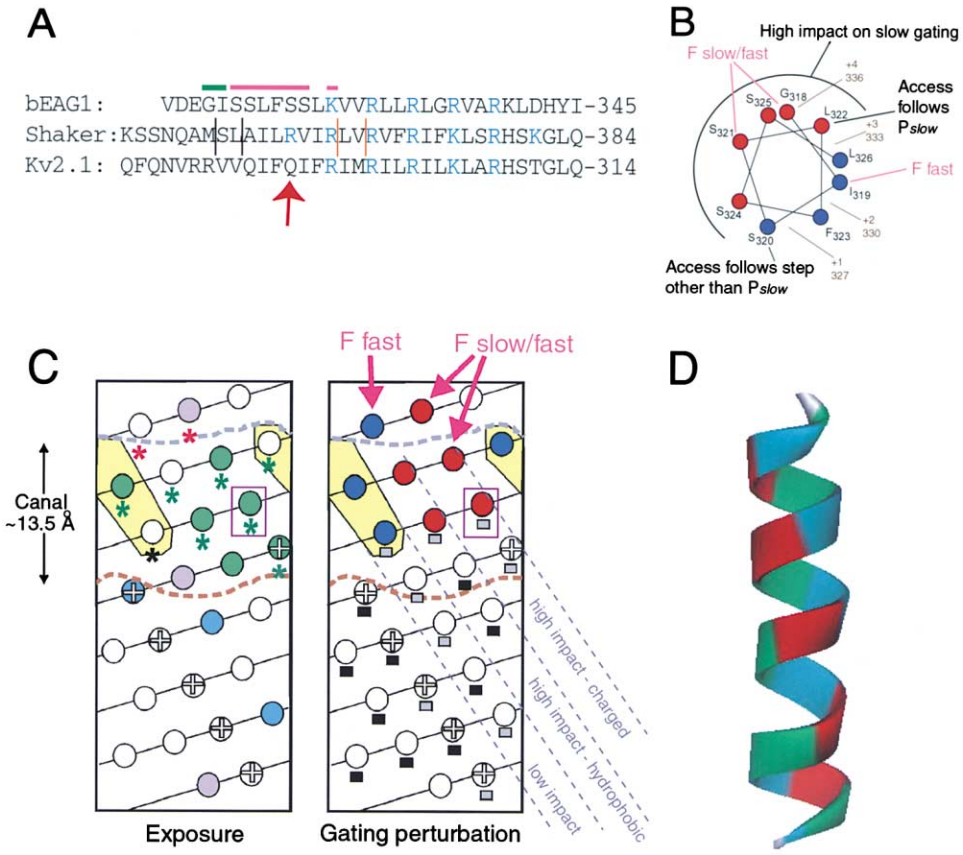

Figure 8. Resting-State S4 Topology

(A) Alignment of bEAG1, Shaker, and Kv2.1 S4s. Resting-state boundary of accessibility to external MTSET for bEAG1 is at transition between residues that are always accessible (green bar) and those accessible only at depolarized potentials (magenta bar; S320-S325 and K327; L326 is either never accessible or else has no impact on gating). Boundaries in Shaker (not defined precisely by Larsson et al., 1996; Baker et al., 1998; Wang et al., 1999) are bracketed by pairs of vertical lines (black, resting state; orange, activated state). Accessibility in bEAG1 and sequence alignment between Shaker and Kv2.1 argue that bEAG1 and Kv2.1 lack Shaker's first basic residue in S4.

(B) Presentation of the results from perturbation analysis and fluorescence measurements on a helical wheel model of S4. Influence of cysteine substitution on slow gating encoded into high- (red) and low-impact (blue) sites, based on the degree of perturbation on the kinetics (Figure 2D) and voltage dependence (Figures 2C and 2E) of P_{slow}. High-impact residues fall on one face of the helix. Fluorescence follows slow gating on high-impact face, but not on low-impact face. The low-impact residues likely face lipid or water at rest. Basic residues are shown in brown, indicating the residue number and the order within S4 (+1 through +4).

(C) Helical net model of S4 resting-state topology in bEAG1 and Shaker (external end up, starting at bEAG1 site 317 and Shaker site 355). (Left) Accessibility of bEAG1 (red asterisk, always external; green asterisk, external only at depolarized potentials; black asterisk, never external or no impact). Accessibility of Shaker to MTSET (Larsson et al., 1996; Baker et al., 1998) and PCMBS (Wang et al., 1999) (filled circles; green, external only at depolarized potentials; cyan, internal only at hyperpolarized potentials; lavender, accessibility constant—always out, in, or inaccessible) superimposed on bEAG1 that lacks the first basic residue (purple box). Accessibility pattern defines external and internal boundaries of the canal (brown/gray dashed lines). (Right) Perturbation of slow gating mode by cysteine mutations in bEAG1. High-impact sites on P_{slow} (red) are in the canal at rest. Low-impact sites (blue) in the canal likely face lipid (yellow). The impact of alanine substitution on Kv2.1's *G-V* (Li-Smerin et al., 2000; high impact, black bars; low impact, gray bars), with Kv2.1, which lacks Shaker's R1 (purple box). bEAG1 S4 sites in the canal *in resting state* impact slow gating, while Kv2.1 sites in the canal in *activated state* impact opening, consistent with S4 outward translation upon activation. Three parallel stripes along S4 (high-impact charged stripe, high-impact hydrophobic stripe, low-impact hydrophobic stripe) are continuous between bEAG1 and Kv2.1, forming three threads of a helical screw.

(D) The three threads colored in red, blue, and green, shown in an α-helical 3D model, are consistent with rotation accompanying translation.

the S4 helix (Figure 8D). Two other faces also make continuous stripes: the high-impact positively charged basic residues and the high-impact hydrophobic face (Figure 8C). The three stripes spiral down S4 in parallel, covering a segment roughly twice as long as the canal. It would be possible to always satisfy S4 energetically in the canal if an axial translation (of the kind that could account for the observed voltage-dependent changes in accessibility) were accompanied by rotation along the pitch of these three threads, with (1) the high-impact positively charged stripe always facing negative counter-charges in S2 and S3, (2) the high-impact hydrophobic stripe always facing into a hydrophobic protein wall of the gating canal (likely including the pore domain), and (3) the low-impact stripe always facing lipid. This model adds two new distinct threads to the charged one on the helical screw proposed by Guy and Seetharamulu (1986) and Catterall (1986).

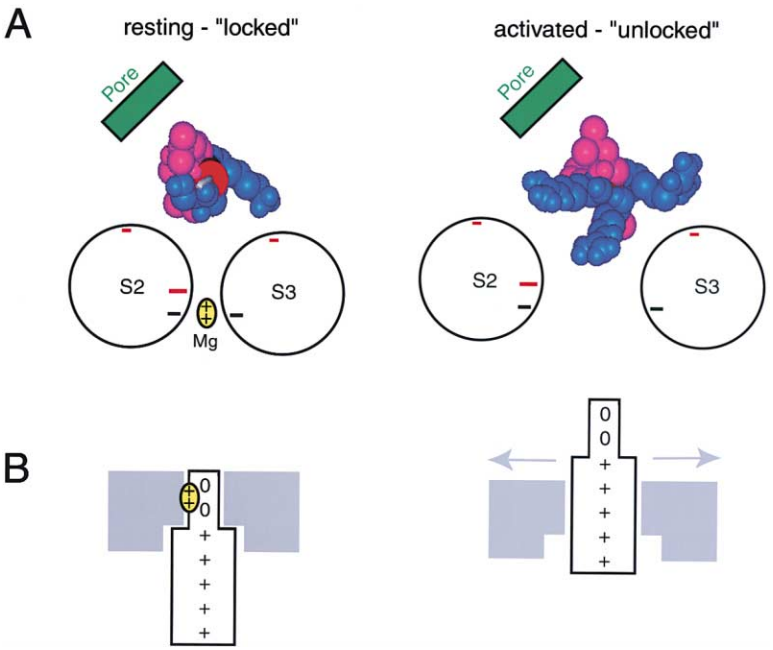

Figure 9. Mg^{+2}-Dependent Canal Rearrangement Proposed to Lock and Unlock S4 in the Resting State

(Left) Mg^{+2} coordination between EAG-specific negative residues in S2 and S3 (black) proposed to lock the canal in a narrow configuration. This configuration can accommodate S4's thin outer end with the high-impact face G-SL-SS-K in the resting state. (Right) Entry of S4's wider section (RL-RL-R) into the canal upon activation demands an "unlocking" motion of S2/S3 (arrows) prior to S4 activation. (A) Top view from the extracellular side shows space-filled side chains for S4's high-impact charged residues (blue) facing S2's and S3's conserved negative residues (larger negative closer to external surface) and high-impact S4's hydrophobic residues (magenta) facing the pore domain. Only high-impact residues located in the canal in the resting (left) or activated state (right) are shown. The activated topology is reached by a 9 residue helical screw motion along the pitch of the threads. (B) Mg^{+2} binding in the canal at rest and unbinding in the activated state would give the canal a constant net charge and could explain the need for stronger hyperpolarization to push S4 into the resting conformation in low $[Mg^{2+}]$.

To account for the observed accessibility changes found here in bEAG1 and earlier in Shaker (Figure 8C), a helical screw motion would displace 9 residues in three ratchet steps, stopping at each position where basic residues in S4 come into register with acidic residues in S2/S3. This motion is striking for its compatibility with several key observations about Shaker: (1) a displacement of ~3 gating charges per subunit (Schoppa et al., 1992); (2) identification of Shaker's outermost arginines, R1–R4, as the primary charge-carrying residues (Aggarwal and MacKinnon, 1996; Seoh et al., 1996; Starace et al., 1997; Starace and Bezanilla, 2001); (3) the 3 + 2 kinetic model of Shaker, which calls for three phases of roughly equal amounts of gating charge displacement per subunit (Schoppa and Sigworth, 1998a, 1998b, 1998c); and (4) a 180° helical rotation of S4 (Cha et al., 1999; Glauner et al., 1999).

Fluorescence from a High-Impact Site follows Slow Transitions

Gating is a function of individual subunits. However, if we analyze currents, we only see the consequence of a concerted action of all four subunits and try to derive information about slow movements from these data. Our original state model proposed that there is an independent transition in each subunit from a fast closed mode to a slow closed mode upon hyperpolarization (Schönherr et al., 1999). Fluorescence analysis has now allowed us to determine directly the movements of single subunits, providing an excellent quantitative correlation with the voltage dependence and kinetics of the ionic current data. We show that TMRM at two sites in the charged high-impact stripe change their fluorescence in parallel to the proposed transition between C_{slow} and C_{fast}. Detailed analysis of channels with the label at 318 revealed close quantitative correlations both in steady-state voltage dependence (left arm of the ΔF-V paralleling the slow gating step, and the right arm of the ΔF-V paralleling the fast activation step) and kinetics (fluorescence following entry and exit from the slow gating mode). These correlations provide direct evidence that a conformational rearrangement of the EAG voltage-sensor domain is responsible for entry into and exit from the slow gating mode. The fact that this rearrangement is detected only on the charged stripe of S4 suggests that the motion is not of S4 but of its protein surround, most likely of S2/S3, as they are thought to interact electrostatically with that face of S4.

A Model for EAG's Voltage-Sensing Domain Rearrangements

Although high-resolution structural data are not available for S1-S4, there is evidence that S1-S3 are helical in Shaker and Kv2.1 and that so is S4 in Kv2.1, with each segment having a lipid face (Hong and Miller, 2000; Li-Smerin et al., 2000). This has led to a four-helix packing model (Li-Smerin et al., 2000) that is compatible with previously identified electrostatic interactions between three conserved acidic residues in S2 and S3 and basic residues in S4 (Papazian et al., 1995; Planells-Cases et al., 1995; Tiwari-Woodruff et al., 1997). According to this model, S1 and S2, with the largest lipid faces, lie at the perimeter of the channel, while S3 and S4 make contacts to pore-forming domain helices S5 and S6. The sandwiching of S4 between S1-S3 and the pore domain agrees with evidence for interaction between S4 and the "turret" at the outer end of S5—an interaction proposed to couple voltage sensing to pore inactivation gating (Gandhi et al., 2000; Larsson and Elinder, 2000; Loots and Isacoff, 2000; Elinder et al., 2001). Using the constraints from the defined Mg^{2+} binding site between two negative charges in S3/S3 and the proposed inter-

actions of negative charges to positive charges in S4, Silverman et al. (2000) proposed a helical packing model of S2, S3, and S4 in *Drosophila* EAG channels, which is compatible with the Shaker and Kv2.1 models. We base our packing cartoon in Figure 9 on this model.

Our accessibility results lead to two striking observations: first, the activated state of EAG has 3 positive S4 residues in the canal, matching the three conserved counter-charges in S2 and S3. But there is only 1 positive S4 residue in the canal at rest (Figure 8C). This could explain our observation that Mg^{2+} enables S4 to reach its resting conformation at less negative voltage, since it may compensate for the missing 2 positive S4 residues in the resting state (Figure 9). Second, the side chain volume of the outer two turns of the S4 helix in EAG is considerably larger (~30%) in the activated state (864 Å^3) than at rest (675 Å^3) (Figure 9A). Since the canal is likely to always be ion and water tight, this argues that the canal must be narrow when S4 is at rest but that it needs to widen in order for S4 to activate. We propose that Mg^{2+} binding is favored by negative voltage in three ways: (1) hyperpolarization pulls Mg^{2+} into the canal; (2) the disappearance from the canal of 2 of the 3 positive residues of S4 favors entry into the canal of Mg^{2+}; (3) narrowing of the canal when the thinner outer end of S4 enters it at rest forms the Mg^{2+} coordination site between S2 and S3 (Figure 9). In this model, Mg^{2+} locks the canal in its narrow conformation and prevents S4 activation sterically and electrostatically, and Mg^{2+} dissociation and canal widening are rate limiting for S4 activation. Mg^{2+}-dependent slow gating is a unique feature of EAG, not even seen in its subfamily member ERG, which also possesses the specialized extra negative residues in S2 and S3. This may be explained by the fact that the outer end of S4 in ERG1 (EELIGLLK) is both thicker than in EAG (SSLFSSLK), and its unique negative charges may repel S2 and S3 in such a way as to keep the canal in its wide conformation when S4 is at rest. Using fluorescence analysis, Smith and Yellen (2002) recently observed fast conformational changes at the outer end of hERG's S4, which occurred in a very hyperpolarized voltage range and could not be correlated to known gating steps but could represent short-lived EAG-like motions of the canal.

Conclusion

Our results provide a molecular mechanism—Mg^{2+}-regulated canal widening—for the control of EAG activation (and thus gating) kinetics. But what do they say about the gating motions of other voltage-gated channels? Although in other K^+ channels the thickness of the portion of S4 that resides in the canal differs by less between the resting and activated states (e.g., the side chains of the outer two turns of S4 are larger in volume in the activated state by ~14% in Shaker, ~9% in Kv2.1), the charge occupancy of the canal changes dramatically, going from one to three positive charges for most K^+ channels, with Shaker exceptionally changing from two to three. This may explain why in all channels S4 relaxes into the activated conformation at 0 voltage. Moreover, it implies that motion of S2 and S3, at least reorientation of negative side chains, may well accompany activation (see Cha and Bezanilla, 1997) and may thus play a role in coupling voltage-sensing motion to gating.

Experimental Procedures

Electrophysiological Measurements

Stage V oocytes were surgically obtained from *Xenopus laevis* under tricaine/ice-water anesthesia. The follicular layer was removed enzymatically, and 50 nl of in vitro transcribed mRNA (0.05–1 μg/μl) was injected. Currents were recorded at 20°C–23°C 1–7 days after injection. For standard two-electrode voltage clamp measurements, a Turbo-TEC 10CD amplifier (NPI electronic, Tamm, Germany) was used, and electrodes filled with 2 M KCl had resistances between 0.5 and 0.9 MΩ. The bath solution (NFR) contained (in mM) 115 NaCl, 2.5 KCl, 1.8 $CaCl_2$, 10 HEPES (pH 7.2) (NaOH). Addition of $MgCl_2$ (5 mM) to this solution is indicated in the figure legends for the respective experiments. Experimental control including pulse generation and data recording was performed with the Pulse+PulseFit software package (HEKA Elektronik, Lambrecht, Germany). For leak correction, a P/n method, supported by Pulse+PulseFit, was used. Data analysis was performed with IgorPro software (WaveMetrics, Lake Oswego, OR). Pooled data are represented as means ± SEM (n = number of independent experiments). For voltage clamp fluorometry experiments, a Dagan CA-1 amplifier (Dagan Corporation, Minneapolis, MN) controlled by the PClamp software package (Axon Instruments, Foster City, CA) was used. MTSET and MTSES (Toronto Research Chemicals, North York, Ontario, Canada) stock solutions were prepared fresh on days of experiments, kept on ice, and directly diluted into bath solution at 20 μM final concentration for cysteine modification.

Fluorescence Measurements

Two-electrode voltage clamp fluorometry was performed as described previously (Mannuzzu et al., 1996; Gandhi et al., 2000). Oocytes were illuminated with a 100 W mercury arc lamp, on a Nikon Diaphot microscope, using a 20 × 0.75 n.a. fluorescence objective (Nikon). Photometry was performed with a Hamamatsu HC120-05 photomultiplier tube. Fluorescence was expressed in photomultiplier output volts relative to fluorescence at the holding potential (set to zero, as a reference). A photomultiplier gain was chosen that made the fluorescence reading at the holding potential 8V. The voltage clamp, photomultiplier, and a Uniblitz shutter (Vincent Associates) were digitized and controlled by a Digidata-1200 board and PClamp7 or a Beta version of PClamp8 software, respectively (Axon Instruments). The excitation light was reduced by neutral density filters (Zeiss, Oberkochen, Germany) with 5% transmission. Light was filtered with a HQ 535/50 excitor, a HQ 610/75 emitter, and a 565LP dichroic (Chroma Technology). The voltage output of the photomultiplier was low-pass filtered at one quarter the sampling frequency with an 8 pole Bessel filter (Frequency Devices). A minimum of a 2 min rest interval at the holding potential of −80mV was given between steps to +40mV.

Data Analysis

Data were analyzed mainly as described previously (Schönherr et al., 1999). In brief, for the description of bEAG1 activation kinetics, it was assumed that each of the four channel subunits undergoes voltage-dependent transitions between two closed states and an activated state: $C_{slow} - C_{fast} - A$. Further assuming that the first transition is slow, the second fast, and both are separated well on the voltage axis, the activation kinetics are roughly described by equation 1 which accounts for a binomial distribution of the subunits among "slow" and "fast" states. P_{slow} denotes the probability of a subunit to reside in C_{slow}; τ_{slow} and τ_{fast} are the time constants for the transitions between $C_{slow} - C_{fast}$ and $C_{fast} - A$, respectively.

$$I(t) = a\left\{(1 - P_{slow})^4(1 - e^{-t\cdot k_f}) + \left[\sum_{i=1}^{4}\binom{4}{i}P_{slow}^{i}(1 - P_{slow})^{4-i}(1 - e^{-t\cdot k_s})^i\right]\right\} \quad (1)$$

In equation 1, a is a current amplitude factor, $k_f = 1/\tau_{fast}$ and $k_s = 1/\tau_{slow}$.

The current-voltage relationships were described by a Boltzmann term for the open-probability and a conductance term obeying the Goldman-Hodgkin-Katz formalism.

$$I(V) = \Gamma V \frac{1 - e^{-(V-E_{rev})/25mV}}{1 - e^{-V/25mV}} (1 + e^{-(V-V_h)/k_h})^{-n} \quad (2)$$

In equation 2, Γ is the total conductance, V the membrane voltage, E_{rev} the reversal potential, V_h the voltage of half-maximal subunit activation, k_h the corresponding slope factor, and n the number of gating units.

Molecular Biology

The bovine *eag*1 gene in the oocyte expression vector pGEM-HE was used for mutagenesis (Schönherr et al., 1999). Point mutations were generated via polymerase chain reaction and subcloned as BstBI-MluI fragments. All constructs were verified by DNA sequencing of this fragment. Following linearization with NheI, mRNA was synthesized in vitro using the T7 mMessage mMachine kit (Ambion, Austin, TX).

Acknowledgments

This work was supported by the Max Planck Society and Deutche Forschungs Gesellshaft (SFB 604, TP A4) grants to S.H.H., and by a National Institutes of Health (R01NS35549) grant to E.Y.I. We thank Chris Gandhi for the results on Shaker S4 labeled with 5′ TMRM; Steffi Arend, Angela Roβner, and Sandra Wiese for technical assistance; and Chris Gandhi, Camin Dean, and Medha Pathak for helpful discussions.

Received: May 9, 2002
Revised: July 17, 2002

References

Aggarwal, S.K., and MacKinnon, R. (1996). Contribution of the S4 segment to gating charge in the *Shaker* K^+ channel. Neuron *16*, 1169–1177.

Baker, O.S., Larsson, H.P., Mannuzzu, L.M., and Isacoff, E.Y. (1998). Three transmembrane conformations and sequence-dependent displacement of the S4 domain in *Shaker* K^+ channel gating. Neuron *20*, 1283–1294.

Baukrowitz, T., and Yellen, G. (1996). Use-dependent blockers and exit rate of the last ion from the multi-ion pore of a K^+ channel. Science *271*, 653–656.

Catterall, W.A. (1986). Voltage-dependent gating of sodium channels: correlating structure and function. Trends Neurosci. *9*, 7–10.

Cha, A., and Bezanilla, F. (1997). Characterizing voltage-dependent conformational changes in the Shaker K^+ channel with fluorescence. Neuron *19*, 1127–1140.

Cha, A., Snyder, G.E., Selvin, P.R., and Bezanilla, F. (1999). Atomic scale movement of the voltage-sensing region in a potassium channel measured via spectroscopy. Nature *402*, 809–813.

Davis, M.D., Wu, X., Nurkiewicz, T.R., Kawasaki, J., Gui, P., Hill, M.A., and Wilson, E. (2001). Regulation of ion channels by protein tyrosine phosphorylation. Am. J. Physiol. Heart Circ. Physiol. *281*, H1835–H1862.

Doyle, D.A., Morais Cabral, J., Pfuetzner, R.A., Kuo, A., Gulbis, J.M., Cohen, S.L., Chait, B.T., and MacKinnon, R. (1998). The structure of the potassium channel: molecular basis of K^+ conduction and selectivity. Science *280*, 69–77.

Elinder, F., Århem, P., and Larsson, H.P. (2001). Localization of the extracellular end of the voltage sensor S4 in a potassium channel. Biophys. J. *80*, 1802–1809.

Frings, S., Brüll, N., Dzeja, C., Angele, A., Hagen, V., Kaupp, U.B., and Baumann, A. (1998). Characterization of *ether-à-go-go* channels present in photoreceptors reveals similarity to I_{KX}, a K^+ current in rod inner segments. J. Gen. Physiol. *111*, 583–599.

Gandhi, C.S., Loots, E., and Isacoff, E.Y. (2000). Reconstructing voltage sensor-pore interaction from a fluorescence scan of a voltage-gated K^+ channel. Neuron *27*, 585–595.

Ganetzky, B., and Wu, C.F. (1983). Neurogenetic analysis of potassium currents in *Drosophila*: synergistic effects on neuromuscular transmission in double mutants. J. Neurogenet. *1*, 17–28.

Glauner, K.S., Mannuzzu, L.M., Gandhi, C.S., and Isacoff, E.Y. (1999). Spectroscopic mapping of voltage sensor movement in the *Shaker* potassium channel. Nature *402*, 813–817.

Guy, H.R., and Seetharamulu, P. (1986). Molecular model of the action potential sodium channel. Proc. Natl. Acad. Sci. USA *83*, 508–512.

Harris, R.E., Larsson, H.P., and Isacoff, E.Y. (1998). A permeant ion binding site between two gates of the *Shaker* K^+ channel. Biophys. J. *74*, 1808–1820.

Herlitze, S., Garcia, D.E., Mackie, K., Hille, B., Scheuer, T., and Catterall, W.A. (1996). Modulation of Ca^{2+} channels by G-protein beta gamma subunits. Nature *380*, 258–262.

Herlitze, S., Zhong, H., Scheuer, T., and Catterall, W.A. (2001). Allosteric modulation of Ca^{2+} channels by G proteins, voltage-dependent facilitation, protein kinase C and Ca(v) beta subunits. Proc. Natl. Acad. Sci. USA *98*, 4699–4704.

Hodgkin, A.L., and Huxley, A.F. (1952). A quantitative description of membrane current and its application to conduction and excitation in nerve. J. Physiol. *117*, 500–544.

Hong, K.H., and Miller, C. (2000). The lipid-protein interface of a *Shaker* K^+ channel. J. Gen. Physiol. *115*, 51–58.

Ikeda, S.R. (1996). Voltage-dependent modulation of N-type calcium channels by G-protein beta gamma subunits. Nature *380*, 255–268.

Jonas, E.A., and Kaczmarek, L.K. (1996). Regulation of potassium channels by protein kinases. Curr. Opin. Neurobiol. *6*, 318–323.

Larsson, H.P., and Elinder, F. (2000). A conserved glutamate is important for slow inactivation in K^+ channels. Neuron *27*, 573–583.

Larsson, H.P., Baker, O.S., Dhillon, D.S., and Isacoff, E.Y. (1996). Transmembrane movement of the *Shaker* K^+ channel S4. Neuron *16*, 387–397.

Li-Smerin, Y., and Swartz, K.J. (2001). Helical structural of the COOH terminus of S3 and its contribution to the gating modifier toxin receptor in voltage-gated ion channels. J. Gen. Physiol. *117*, 205–217.

Li-Smerin, Y., Hackos, D.H., and Swartz, K.J. (2000). α-Helical structural elements within the voltage-sensing domains of a K^+ channel. J. Gen. Physiol. *115*, 33–49.

Liu, Y., Jurman, M.E., and Yellen, G. (1996). Dynamic rearrangement of the outer mouth of a K^+ channel during gating. Neuron *16*, 859–867.

Liu, Y.-S., Sompornpisut, P., and Perozo, E. (2001). Structure of the KcsA channel intracellular gate in the open state. Nat. Struct. Biol. *8*, 883–887.

Loots, E., and Isacoff, E.Y. (2000). Molecular coupling of S4 to a K^+ channeĺs slow inactivation gate. J. Gen. Physiol. *116*, 623–636.

Lopez, G.A., Yan, Y.N., and Yan, L.Y. (1991). Hydrophobic substitution mutations in the S4 sequence alter voltage-dependent gating in Shaker K^+ channels. Neuron *7*, 327–336.

Ludwig, J., Terlau, H., Wunder, F., Brüggemann, A., Pardo, L.A., Marquardt, A., Stühmer, W., and Pongs, O. (1994). Functional expression of a rat homologue of the voltage gated *ether à go-go* potassium channel reveals differences in selectivity and activation kinetics between the *Drosophila* channel and its mammalian counterpart. EMBO J. *13*, 4451–4458.

Ludwig, J., Weseloh, R., Karschin, C., Liu, Q., Netzer, R., Engeland, B., Stansfeld, C., and Pongs, O. (2000). Cloning and functional expression of rat eag2, a new member of the ether-a-go-go family of potassium channels and comparison of its distribution with that of eag1. Mol. Cell. Neurosci. *16*, 59–70.

Mannuzzu, L.M., Moronne, M.M., and Isacoff, E.Y. (1996). Direct physical measure of conformational rearrangement underlying potassium channel gating. Science *271*, 213–216.

Morais-Cabral, J.H., Zhou, Y., and MacKinnon, R. (2001). Energetic optimization of ion conduction rate by the K^+ selectivity filter. Nature *414*, 37–42.

Occhiodoro, T., Bernheim, L., Liu, J.-H., Bijlenga, P., Sinnreich, M., Bader, C.R., and Fischer-Lougheed, J. (1998). Cloning of a human *ether à go-go* potassium channel expressed in myoblasts at the onset of fusion. FEBS Lett. *434*, 177–182.

Papazian, D.M., Shao, X.M., Seoh, S.-A., Mock, A.F., Huang, Y., and Wainstock, D.H. (1995). Electrostatic interactions of S4 voltage sensor in *Shaker* K^+ channels. Neuron *14*, 1293–1301.

Perozo, E., Cortes, D.M., and Cuello, L.G. (1999). Structural rearrangements underlying K^+-channel activation gating. Science *285*, 73–78.

Planells-Cases, R., Ferrer-Montiel, A.V., Patten, C.D., and Montal, M. (1995). Mutation of conserved negatively charged residues in the S2 and S3 transmembrane sements of a mammalian K^+ channel selectively modulates channel gating. Proc. Natl. Acad. Sci. USA *92*, 9422–9426.

Saganich, M.J., de Miera, E.V.-S., Nadal, M.S., Baker, H., Coetzee, W.A., and Rudy, B. (1999). Cloning of components of a novel subthreshold-activating K^+ channel with a unique pattern of expression in the cerebral cortex. J. Neurosci. *19*, 10789–10802.

Schönherr, R., Hehl, S., Terlau, H., Baumann, A., and Heinemann, S.H. (1999). Individual subunits contribute to slow gating of bovine EAG potassium channels. J. Biol. Chem. *274*, 5362–5369.

Schönherr, R., Löber, K., and Heinemann, S.H. (2000). Inhibition of human *ether à go-go* potassium channels by Ca^{2+}/calmodulin. EMBO J. *19*, 3263–3271.

Schönherr, R., Gessner, G., Löber, K., and Heinemann, S.H. (2002). Functional distinction of human EAG1 and EAG2 potassium channels. FEBS Lett. *514*, 204–208.

Schoppa, N.E., and Sigworth, F.J. (1998a). Activation of Shaker potassium channels. I. Characterization of voltage-dependent transitions. J. Gen. Physiol. *111*, 271–294.

Schoppa, N.E., and Sigworth, F.J. (1998b). Activation of Shaker potassium channels. II. Kinetics of the V2 mutant channel. J. Gen. Physiol. *111*, 295–311.

Schoppa, N.E., and Sigworth, F.J. (1998c). Activation of Shaker potassium channels. III. An activation gating model for wild-type and V2 mutant channels. J. Gen. Physiol. *111*, 313–342.

Schoppa, N.E., McCormack, K., Tanouye, M.A., and Sigworth, F.J. (1992). The size of gating charge in wild-type and mutant *Shaker* potassium channels. Science *255*, 1712–1715.

Seoh, S.-A., Sigg, D., Papazian, D.M., and Bezanilla, F. (1996). Voltage-sensing residues in the S2 and S4 segments of the *Shaker* K^+ channel. Neuron *16*, 1159–1167.

Silverman, W.R., Tang, C.-Y., Mock, A.F., Huh, K.-B., and Papazian, D.M. (2000). Mg^{2+} modulates voltage-dependent activation in *ether-à-go-go* potassium channels by binding between transmembrane segments S2 and S3. J. Gen. Physiol. *116*, 663–677.

Smith, P., and Yellen, G. (2002). Fast and slow voltage sensor movements in HERG potassium channels. J. Gen. Physiol. *119*, 275–293.

Starace, D.M., and Bezanilla, F. (2001). Histidine scanning mutagenesis of basic residues of the S4 segment of the Shaker K^+ channel. J. Gen. Physiol. *117*, 469–490.

Starace, D.M., Stefani, E., and Bezanilla, F. (1997). Voltage-dependent proton transport by the voltage sensor of the *Shaker* K^+ channel. Neuron *19*, 1319–1327.

Tang, C.-Y., Bezanilla, F., and Papazian, D.M. (2000). Extracellular Mg^{2+} modulates slow gating transitions and the opening of *Drosophila ether-à-go-go* potassium channels. J. Gen. Physiol. *115*, 319–337.

Terlau, H., Ludwig, J., Steffan, R., Pongs, O., Stühmer, W., and Heinemann, S.H. (1996). Extracellular Mg^{2+} regulates activation of rat *eag* potassium channel. Pflugers Arch. *432*, 301–312.

Tiwari-Woodruff, S.K., Schulteis, C.T., Mock, A.F., and Papazian, D.M. (1997). Electrostatic interactions between transmembrane segments mediate folding of *Shaker* K^+ channel subunits. Biophys. J. *72*, 1489–1500.

Wang, M.H., Yusaf, S.P., Elliott, D.J., Wray, D., and Sivaprasadarao, A. (1999). Effect of cysteine substitutions on the topology of the S4 segment of the Shaker potassium channel: implications for molecular models of gating. J. Physiol. *521*, 315–326.

Yang, N., and Horn, R. (1995). Evidence for voltage-dependent S4 movement in sodium channels. Neuron *15*, 213–218.

Yang, N., George, A.L., Jr., and Horn, R. (1996). Molecular basis of charge movement in voltage-gated sodium channels. Neuron *16*, 113–122.

Yellen, G. (1998). The moving parts of ion channels. Q. Rev. Biophys. *31*, 239–296.

Yusaf, S.P., Wray, D., and Sivaprasadarao, A. (1996). Measurement of the movement of the S4 segment during the activation of a voltage-gated potassium channel. Pflugers Arch. *433*, 91–97.

Zagotta, W.N., Hoshi, T., and Aldrich, R.W. (1994). *Shaker* potassium channel gating. III: Evaluation of kinetic models for activation. J. Gen. Physiol. *103*, 321–362.